International Communications in Heat and Mass Transfer 140 (2023) 106482

Contents lists available at ScienceDirect

International Communications in Heat and Mass Transfer

journal homepage: www.elsevier.com/locate/ichmt

Heat transfer in a multi-layered semiconductor device with spatially-varying thermal contact resistance between layers

Girish Krishnan, Ankur Jain *

Mechanical and Aerospace Engineering Department, University of Texas at Arlington, Arlington, TX, USA

ARTICLE INFO

Keywords:
Semiconductor thermal management
Thermal contact resistance
Analytical modeling

ABSTRACT

Thermal management of multilayer microelectronic devices such as three-dimensional integrated circuits remains an important technological challenge. In such systems, inter-layer thermal contact resistance may vary spatially due to spatial variation in bond pad density and size. However, past theoretical heat transfer models mostly assume perfect thermal contact between adjacent layers, or, at most, uniform thermal contact resistance. This work presents a theoretical model to determine the steady state temperature distribution in a general *M*-layer structure with spatial variation in thermal contact resistance between adjacent layers. An infinite series solution is derived, for which, once truncated to a finite number of terms, the coefficients are determined from algebraic equations derived from the given spatially varying thermal contact resistances. Results for the special case of a two-layer body are presented. It is shown that the degree of alignment between heat flux and thermal contact resistance distributions plays a key role in determining the overall temperature distribution. Compared to numerical simulations, the analytical technique offers more efficient computation, and a better fundamental understanding of the problem. This work contributes towards improved thermal design tools for multilayer semiconductor devices. The theoretical technique developed here may find applications in other heat transfer problems as well.

1. Introduction

Heat removal from semiconductor devices and systems continues to remain a key technological challenge that often limits performance and reliability [1,2]. Heat generated during the operation of a semiconductor device must be efficiently removed in order to minimize chip temperature rise. A variety of thermal management techniques have been used, ranging from passive cooling for low power chips [3], to air cooling aided by heat sinks for medium power chips [4] and advanced techniques such as liquid [5] and two-phase cooling [1] for high-power chips.

The thermal management challenge in semiconductor devices has been exacerbated by recent advances in heterogeneous integration in chip and package level architecture [2,6,7]. For example, the bonding of multiple dies to produce three-dimensional integrated circuits (3D ICs) offers several important electrical benefits [8], contributing towards continuation of Moore's law [9], but also leads to significant thermal contact resistance between dies [10,11], which may increase total temperature rise in the chip [12]. The use of dis-similar materials in different dies (heterogeneous integration, such as memory-on-logic chips) or within a single die (due to the use of through-silicon vias (TSVs)) also presents thermal management challenges.

In this context, one specific problem of interest is that of interfacial thermal contact resistance between adjacent layers in a multi-die stack. Typically, adjacent layers are bonded to each other by depositing metal pads on the mating surfaces. These pads, usually made of Copper, Tin or similar metals are then aligned and pressed on to each other at high temperature and pressure to form a metal-to-metal bond [13–15]. Such a bond provides mechanical integration and electrical interconnection. The region surrounding the bond pads may be filled with a low thermal conductivity epoxy, or may simply remain unfilled. In addition, such metal-to-metal bonding often results in the formation of low thermal conductivity eutectics [14]. These factors may all contribute towards significant interfacial thermal contact resistance between adjacent die. Past papers have measured this thermal contact resistance [10,11,16], although measured values are averages over the entire bonded surface, and spatial variation in thermal contact resistance has not been characterized. Such spatial variation may arise from variation in the number and size of metal pads from one part of the interface to the other, in order to cater to inter-die electrical interconnection requirements in different blocks. For example, some regions may contain a large number

* Corresponding author.
E-mail address: jaina@uta.edu (A. Jain).

https://doi.org/10.1016/j.icheatmasstransfer.2022.106482

Nomenclature

Bi	Biot number, $Bi = \frac{hz_M}{k_M}$
h	convective heat transfer coefficient ($Wm^{-2}\ K^{-1}$)
k	thermal conductivity ($Wm^{-1}\ K^{-1}$)
$\bar{k}$	non-dimensional thermal conductivity, $\bar{k}_m = \frac{k_m}{k_M}$
M	number of layers
N	number of eigenvalues
q''	heat flux (Wm^{-2})
R	spatially varying thermal contact resistance (Km^2W^{-1})
T	temperature (K)
w	width of the body in the y direction (m)
$\bar{g}$	non-dimensional thermal contact resistance, $\bar{g}_m(\eta) = \frac{R_m(y)k_M}{z_M}$
$\bar{q}$	non-dimensional heat flux, $\bar{q}(\eta) = \frac{q''(y)z_M}{k_M(T_{ref}-T_{amb})}$
$\bar{w}$	non-dimensional width of the body in the y direction, $\bar{w} = \frac{w}{z_M}$
y, z	spatial coordinates (m)
η, ξ	non-dimensional spatial coordinates, $\eta = \frac{y}{z_M}; \xi = \frac{z}{z_M}$
γ	non-dimensional interface location, $\gamma_m = \frac{z_m}{z_M}$
θ	non-dimensional temperature, $\theta_m = \frac{T_m-T_{amb}}{T_{ref}-T_{amb}}$
λ	non-dimensional eigenvalue

Subscripts

amb	ambient
m	layer number
M	total number of layers
ref	reference

of bond pads and/or bond pads of larger size, depending on TSV size and current requirements, and therefore may have lower thermal contact resistance locally. Such variation in interfacial thermal contact resistance is clearly important to account for in thermal management design, since, for example, heat will travel more easily through regions with low interfacial thermal contact resistance, and may be heavily impeded where interfacial thermal contact resistance is high, leading to thermal gradients within the chips, and possibly larger peak temperature rise.

Unfortunately, thermal models for heat transfer in 3D ICs account for, at most, a uniform thermal contact resistance [12,17,18]. Developing more sophisticated heat transfer models for a multidie stack with spatially-varying thermal contact resistance between layers may not only help understand the fundamental nature of this problem, but may also help in experimental design, such as in thermally optimal placement and sizing of TSVs and/or inter-die bond pads [19,20]. Experimental measurements are often limited by costs and complexity. Theoretical models can help evaluate multiple designs even before manufacturing, and thus, maximize the benefit of thermal test vehicles.

Theoretical heat transfer modeling in semiconductor chips often involves developing exact, closed-form solutions to differential equations that govern the temperature field in the chip based on the principle of energy conservation [12,17,18]. Theoretical analysis offers several advantages and a few limitations compared to numerical simulations, as summarized in Table 1. Such closed-form solutions have been derived for a wide variety of problems in multilayer problems, including for thermal conduction in a multi-die chip stack with constant [18] or spatially varying [21] convective heat transfer coefficient, stacks of unequally sized die [22], etc. Even when such models account for inter-die thermal contact resistance, they do so only as a uniform quantity over the entire die surface. The introduction of a spatially-dependent contact resistance makes it difficult to solve this problem using standard methods such as separation of variables, because when the contact resistance is a function of space, explicit expressions for the coefficients can no longer be determined using the principle of orthogonality. There is a lack of analytical methods in the literature to account for spatial variation in inter-die thermal contact resistance, which, as summarized above, may play an important role in thermal management of multilayer chip stacks. While analytical methods to account for spatial variation in convective heat transfer coefficient have been applied in the past for analyzing heat transfer in fins [23], cylinders [24], as well as for multilayer bodies [21], there does not appear to be much literature on modeling of spatial variation in thermal contact resistance in semiconductor chips.

Table 1
Comparison of relative advantages and disadvantages of theoretical thermal conduction analysis and numerical simulations.

	Theoretical analysis	Numerical simulations
Advantages	• May offer exact solution. • May compute faster.	• May be easier to set up. • May be able to account for several secondary effects.
Disadvantages	• May be more difficult to derive. • May not easily be able to account for secondary effects such as temperature-dependent properties.	• May incur greater error. • May be more time consuming.

This work presents theoretical analysis of the problem of thermal conduction in a multi-die chip stack with spatial variation in interfacial thermal contact resistance between layers. It is shown that an eigenfunction-based series solution for this problem may be obtained, and coefficients occurring in the series may be determined to account for the various boundary and interface conditions. Specifically, a system of linear algebraic equations for the unknown coefficients may be derived in order to account for the spatially varying thermal contact resistance. A general M-layer problem is first solved, followed by illustration of a specific two-layer problem. The resulting closed-form solution for the temperature distribution is shown to agree well with numerical simulations, and is used to develop a fundamental understanding of the nature of thermal transport in this problem. The solution is used for analyzing practical problems in semiconductor thermal management.

The next section defines the problem considered in this work, and then outlines a theoretical solution for the problem. Section 3 discusses key results based on this theoretical model. Concluding remarks, including limitations of the present work and possible future work are given in Section 4.

2. Mathematical modeling

2.1. Description of the problem

Consider the problem of steady-state thermal conduction in an M-layer geometry as shown in Fig. 1(a). Each layer has a given thermal conductivity, k_m, assumed to be constant and uniform for each layer, $m = 1,2,..\ M$. For simplicity, the geometry is taken to be two-dimensional, although extension to three-dimensional geometry is quite straightforward. The sidewalls are assumed to be adiabatic, as is commonly the case due to the thin nature of semiconductor devices [18]. As shown in Fig. 1(a), the width of the geometry is w, and thickness of the m^{th} layer is z_m-z_{m-1}. Total thickness of the multilayer body is z_M. As is commonly the case with semiconductor devices, a general convective heat transfer boundary condition, characterized by a constant convective heat transfer coefficient h is assumed on the bottom surface. On the top surface, a spatially varying heat flux $q(y)$ is assumed in order to model

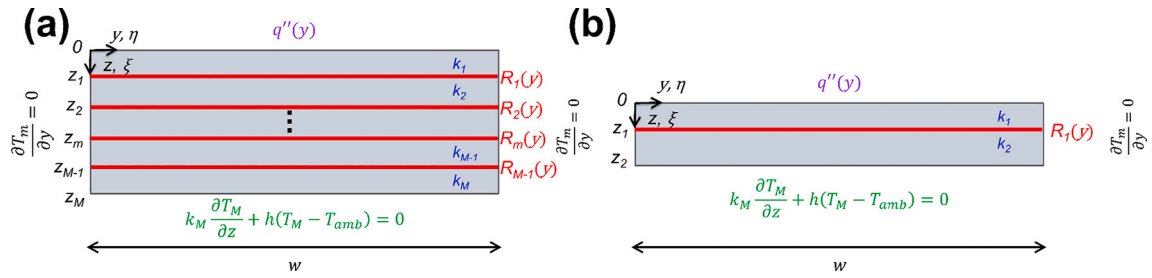

Fig. 1. Schematic of the (a) *M*-layer and (b) two-layer geometry representative of a multilayer semiconductor chip with *y*-dependent thermal contact resistance at each interface.

spatial variation in heat generation in semiconductor devices due to distribution of heat loads in various functional blocks on the chip. A heat flux boundary condition is appropriate for modeling this phenomenon because heat generated in the functional blocks enters the geometry under consideration. Finally, a spatially varying thermal contact resistance $R_m(y)$ is assumed at the interface between the m^{th} and $(m+1)^{th}$ layers ($m = 1,2,..M\text{-}1$). These contact resistances, in general, depend on the nature of the individual interfaces, and need not be equal to each other. Assuming all properties are independent of temperature, the interest is in determining the steady-state temperature distribution, and, in particular, the peak temperature rise.

The general *M*-layer problem is considered first, followed by discussion of the special case of a two-layer body containing a single interface. Based on the problem description and assumptions discussed above, the next sub-section defines the problem mathematically. Non-dimensionalization is then carried out, followed by an outline of the solution procedure.

2.2. Problem definition and non-dimensionalization

Based on the problem description above, the steady-state temperature rise in the *M*-die stack, $T_m(y,z)$ is governed by the following energy conservation equation:

$$\frac{\partial^2 T_m}{\partial y^2} + \frac{\partial^2 T_m}{\partial z^2} = 0 \quad (z_{m-1} < z < z_m; 0 < y < w) \tag{1}$$

for $m = 1,2..M$.

Associated boundary conditions in the z direction are

$$-k_1 \frac{\partial T_1}{\partial z} = q''(y) \quad (z = 0) \tag{2}$$

and

$$-k_M \frac{\partial T_M}{\partial z} + h(T_M - T_{amb}) = 0 \quad (z = z_M) \tag{3}$$

In addition, heat flux must be conserved at each interface, i.e.,

$$-k_m \frac{\partial T_m}{\partial z} = -k_{m+1} \frac{\partial T_{m+1}}{\partial z} \quad (z = z_m) \tag{4}$$

for $m = 1,2..M\text{-}1$.

The following equation may be written to model the spatially-varying thermal contact resistance at each interface.

$$T_m = T_{m+1} - k_m \frac{\partial T_m}{\partial z} R_m(y) \quad (z = z_m) \tag{5}$$

for $m = 1,2..M\text{-}1$.

Here, $R_m(y)$ is the spatially varying thermal contact resistance at the m^{th} interface. Note that the thermal contact resistance is defined as the ratio of temperature difference and heat flux across the interface [25,26]. Eq. (5) expresses this in a spatially varying form. The larger the thermal contact resistance, for example, due to imperfect contact, the larger is the temperature difference. In the ideal scenario of perfect contact, the thermal contact resistance is zero, and, therefore, there is no temperature jump across the interface.

In the *y* direction, adiabatic conditions are assumed along the side walls, as is commonly assumed for semiconductor chips [12,17,18].

$$\frac{\partial T_m}{\partial y} = 0 \quad (y = 0, w) \tag{6}$$

for m=1,2,..*M*.

Eqs. (1)–(6)define the problem of interest here. In order to generalize the results from this work, non-dimensionalization is first carried out based on the following variables:

$$\theta_m = \frac{T_m - T_{amb}}{T_{ref} - T_{amb}}; \xi = \frac{z}{z_M}, \eta = \frac{y}{z_M}, \gamma_m = \frac{z_m}{z_M}; \bar{w} = \frac{w}{z_M}; \bar{k}_m = \frac{k_m}{k_M}; Bi = \frac{h z_M}{k_M} \tag{7}$$

where T_{ref} ($\neq T_{amb}$) is a reference temperature.

Inserting the non-dimensional variables in eqs. (1)–(6) results in the following set of non-dimensional equations, boundary conditions and interface conditions.

$$\frac{\partial^2 \theta_m}{\partial \eta^2} + \frac{\partial^2 \theta_m}{\partial \xi^2} = 0 \quad (\gamma_{m-1} < \xi < \gamma_m; 0 < \eta < \bar{w}) \tag{8}$$

$$-\bar{k}_1 \frac{\partial \theta_1}{\partial \xi} = \bar{q}(\eta) \quad (\xi = 0) \tag{9}$$

$$\bar{k}_M \frac{\partial \theta_M}{\partial \xi} + Bi \cdot \theta_M = 0 \quad (\xi = 1) \tag{10}$$

$$\bar{k}_m \frac{\partial \theta_m}{\partial \xi} = \bar{k}_{m+1} \frac{\partial \theta_{m+1}}{\partial \xi} \quad (\xi = \gamma_m) \tag{11}$$

$$\theta_m = \theta_{m+1} - \bar{k}_m \frac{\partial \theta_m}{\partial \xi} \bar{g}_m(\eta) \quad (\xi = \gamma_m) \tag{12}$$

$$\frac{\partial \theta_m}{\partial \eta} = 0 \quad (\eta = 0, \bar{w}) \tag{13}$$

where $\bar{q}(\eta) = q''(y) z_M / \left(k_M (T_{ref} - T_{amb})\right)$ and $\bar{g}_m(\eta) = R_m(y) k_M / z_M$ are the non-dimensional heat flux at the bottom face and non-dimensional thermal contact resistance at the m^{th} interface, respectively. Both are, in general, functions of η. While the spatial dependence of the heat flux can be easily accounted for using the principle of orthogonality of eigenfunctions, modeling the spatial dependence of the thermal contact resistance is not straightforward, especially due to the large number of interfaces. An analytical solution for this problem is presented in the next section.

2.3. Analytical solution of the M-layer problem

If the contact resistances $\bar{g}_m$ were constants, this problem could be easily solved using the separation of variables method, including the

determination of the coefficients in the series solution using the principle of orthogonality. In the present case, however, this simple technique is not applicable due to the spatial dependence of $\bar{g}_m$. Here, the temperature distributions in the layers are written in an infinite series form, which is truncated for computation up to a finite number of terms. Then, instead of explicit expressions for the unknown coefficients, as is the case in standard separation of variables method, a sufficient number of linear algebraic equations based on the boundary and interface conditions are derived, using which, the coefficients can be determined. To begin with, a general solution for temperature distribution in the m^{th} layer may be written as

$$\theta_m(\xi,\eta) = c_{m,0}(\xi) + \sum_{n=1}^{\infty} c_{m,n}(\xi)cos(\lambda_n\eta) \tag{14}$$

where $\lambda_n = \frac{n\pi}{\bar{w}}$ are the eigenvalues. Only cosine terms are considered in eq. (14) in order to satisfy the adiabatic boundary conditions at $\eta = 0$ and $\eta = \bar{w}$. Note that $n = 0$ is included in eq. (14) because both boundary conditions in η direction are adiabatic [27].

Now, in order for eq. (14) to satisfy the governing equation given by eq. (1), $c_{m,0}$ and $c_{m,n}$ must satisfy $c''_{m,0} = 0$ and $c''_{m,n} = -\lambda_n^2 c_{m,n} (n = 1,\ldots,\infty)$. Therefore, one may write

$$c_{m,0} = A_{m,0} + B_{m,0}\xi \tag{15}$$

$$c_{m,n} = A_{m,n}cosh(\lambda_n\xi) + B_{m,n}sinh(\lambda_n\xi) \tag{16}$$

where, for each layer, $A_{m,0}$, $B_{m,0}$, $A_{m,n}$ and $B_{m,n}$ are all unknown coefficients to be determined in order to complete the solution. In addition, while in principle, the solution is an infinite series, in practice, a sufficiently large but finite number of terms must be considered for computation. Denoting the number of terms considered by N, the total number of unknown coefficients to be determined in order to complete the solution is given by $2(N+1)M$ ($A_{m,0}$, $A_{m,1}$, $A_{m,2}$, $A_{m,3}$,.. $A_{m,N}$ and $B_{m,0}$, $B_{m,1}$, $B_{m,2}$, $B_{m,3}$,.. $B_{m,N}$ for each layer 1,2.3…M). These coefficients are determined through derivation of $2(N+1)M$ linear algebraic equations in these unknowns using the boundary and interface conditions.

To begin with, the use of the heat flux boundary condition at $\xi = 0$, eq. (9) results in

$$\bar{k}_1\left(B_{1,0} + \sum_{n=1}^{N}\lambda_n B_{1,n}\cos(\lambda_n\eta)\right) = -\bar{q}(\eta) \tag{17}$$

from where, based on Fourier series expansion of $\bar{q}(\eta)$, one may write

$$B_{1,0} = -\frac{1}{\bar{k}_1\bar{w}}\int_0^{\bar{w}}\bar{q}(\eta^*)d\eta^* \tag{18}$$

$$B_{1,n} = -\frac{2}{\bar{k}_1\bar{w}\lambda_n}\int_0^{\bar{w}}\bar{q}(\eta^*)cos(\lambda_n\eta^*)d\eta^* \tag{19}$$

which are a total of $(N+1)$ equations. Further, from the convective boundary condition at $\xi = 1$ given by eq. (10), one may write

$$B_{M,0} + \sum_{n=1}^{N}\lambda_n\left(A_{M,n}sinh(\lambda_n) + B_{M,n}cosh(\lambda_n)\right)cos(\lambda_n\eta) + Bi\left[A_{M,0} + B_{M,0} + \sum_{n=1}^{N}\left(A_{M,n}cosh(\lambda_n) + B_{M,n}sinh(\lambda_n)\right)cos(\lambda_n\eta)\right] = 0 \tag{20}$$

A term-by-term comparison results in the following $(N+1)$ equations

$$(1+Bi)B_{M,0} + BiA_{M,0} = 0 \tag{21}$$

$$A_{M,n}(\lambda_n sinh(\lambda_n) + Bicosh(\lambda_n)) + B_{M,n}(\lambda_n cosh(\lambda_n) + Bisinh(\lambda_n)) = 0 \tag{22}$$

In addition to the $2(N+1)$ equations derived above, the interface conditions may be used to derive the additional equations needed to complete the set of $2(N+1)M$ equations. Consider the m^{th} interface between m^{th} and $(m+1)^{th}$ layers (m = 1,2..M-1). Based on heat flux conservation at this interface, given by eq. (11), one may write

$$\bar{k}_m\left[B_{m,0} + \sum_{n=1}^{N}\lambda_n\left(A_{m,n}sinh(\lambda_n\gamma_m) + B_{m,n}cosh(\lambda_n\gamma_m)\right)cos(\lambda_n\eta)\right] = \bar{k}_{m+1}\left[B_{m+1,0} + \sum_{n=1}^{N}\lambda_n\left(A_{m+1,n}sinh(\lambda_n\gamma_m) + B_{m+1,n}cosh(\lambda_n\gamma_m)\right)cos(\lambda_n\eta)\right] \tag{23}$$

A term-by-term comparison results in

$$\bar{k}_m B_{m,0} = \bar{k}_{m+1}B_{m+1,0} \tag{24}$$

$$\bar{k}_m\left(A_{m,n}sinh(\lambda_n\gamma_m) + B_{m,n}cosh(\lambda_n\gamma_m)\right) = \bar{k}_{m+1}\left(A_{m+1,n}sinh(\lambda_n\gamma_m) + B_{m+1,n}cosh(\lambda_n\gamma_m)\right) \tag{25}$$

Note that eqs. (24) and (25) apply at each interface, i.e., m = 1,2..M-1, and therefore constitute a total of $(N+1)(M\text{-}1)$ equations.

Finally, the interface conditions involving the spatially varying thermal contact resistances are utilized to derive the remaining equations. Based on eq. (12) at the m^{th} interface, one may write

$$A_{m,0} + B_{m,0}\gamma_m + \sum_{n=1}^{N}\left(A_{m,n}cosh(\lambda_n\gamma_m) + B_{m,n}sinh(\lambda_n\gamma_m)\right)cos(\lambda_n\eta) = A_{m+1,0} + B_{m+1,0}\gamma_m + \sum_{n=1}^{N}\left(A_{m+1,n}cosh(\lambda_n\gamma_m) + B_{m+1,n}sinh(\lambda_n\gamma_m)\right)cos(\lambda_n\eta) - \bar{k}_m\bar{g}_m(\eta)\left[B_{m,0} + \sum_{n=1}^{N}\lambda_n\left(A_{m,n}sinh(\lambda_n\gamma_m) + B_{m,n}cosh(\lambda_n\gamma_m)\right)cos(\lambda_n\eta)\right] \tag{26}$$

Eq. (26) is multiplied by $\cos(\lambda_{n'}\eta)$ for $n' = 0, 1, 2..\ N$ and integrated from $\eta = 0$ to $\eta = \bar{w}$. For $n' = 0$, i.e., λ_0=0, this results in

$$\left(A_{m,0} + B_{m,0}\gamma_m\right)\bar{w} = \left(A_{m+1,0} + B_{m+1,0}\gamma_m\right)\bar{w} - \bar{k}_m B_{m,0}\int_0^{\bar{w}}\bar{g}_m(\eta^*)d\eta^* - \sum_{n=1}^{N}\bar{k}_m\lambda_n\left(A_{m,n}sinh(\lambda_n\gamma_m) + B_{m,n}cosh(\lambda_n\gamma_m)\right)\int_0^{\bar{w}}\bar{g}_m(\eta^*)cos(\lambda_n\eta^*)d\eta^* \tag{27}$$

and for $n' = 1, 2..\ N$, one may obtain, based on the principle of orthogonality

$$\left(A_{m,n'}cosh(\lambda_{n'}\gamma_m)+B_{m,n'}sinh(\lambda_{n'}\gamma_m)\right)N_{n'}=\left(A_{m+1,n'}cosh(\lambda_{n'}\gamma_m)+B_{m+1,n'}sinh(\lambda_{n'}\gamma_m)\right)N_{n'}-\bar{k}_mB_{m,0}\int_0^{\bar{w}}\bar{g}_m(\eta^*)cos(\lambda_{n'}\eta^*)d\eta^*-\sum_{n=1}^{N}\bar{k}_m\lambda_n\left(A_{m,n}sinh(\lambda_n\gamma_m)+B_{m,n}cosh(\lambda_n\gamma_m)\right)\int_0^{\bar{w}}\bar{g}_m(\eta^*)cos(\lambda_{n'}\eta^*)cos(\lambda_n\eta^*)d\eta^* \tag{28}$$

where $N_{n'}=\frac{\bar{w}}{2}$ is the eigenfunction norm. Eqs. (27)–(28) constitute $(N+1)$ equations per interface, and thus, a total of $(M\text{-}1)(N+1)$ equations. Therefore, the set of eqs. (18), (19), (21), (22), (24), (25), (27) and (28) together constitute $2(N+1)M$ equations, which is the precise number of unknown coefficients needed to be determined. Therefore, the set of linear algebraic equations represented by these equations can be solved to determine a solution for the temperature distributions in each layer for a general M-layer problem. While an exact solution for these linear equations is unlikely, nevertheless, these equations can be easily solved through matrix inversion.

3. Special case: two-layer body with single interface

The case of a two-layer body with a single interface is of particular interest, since such a geometry appears commonly in semiconductor thermal management as well as in other engineering problems. While, in principle, the results for this case can be obtained by using $M = 2$ in section 2.3, it is instructive to solve this problem explicitly.

The two-layer geometry is shown in Fig. 1(b). In this case, there exists a single interface at $\xi = \gamma_1$, along which, the thermal contact resistance is denoted by $\bar{g}_1(\eta)$. The temperature distributions in the two layers is given by

$$\theta_m(\xi\eta)=A_{m,0}+B_{m,0}\xi+\sum_{n=1}^{\infty}\left[A_{m,n}cosh(\lambda_n\xi)+B_{m,n}sinh(\lambda_n\xi)\right]cos(\lambda_n\eta) \tag{29}$$

for m=1, 2. Similar to section 2.3, up to $n = N$ eigenvalues are considered for this problem. Therefore, a total of $4(N + 1)$ unknown coefficients need to be determined – $A_{1,0}$, $B_{1,0}$, $A_{2,0}$, $B_{2,0}$ and $A_{1,n}$, $B_{1,n}$, $A_{2,n}$, $B_{2,n}$ for n = 1,2..N. These may be determined using boundary and interface conditions associated with this problem. From the boundary condition at ξ = 0, one may obtain $B_{1,0}$ and $B_{1,n}$, as given by eqs. (18) and (19). Further, using the boundary condition at $\xi = 1$, one may write $B_{2,0} = p_0A_{2,0}$ and $B_{2,n} = p_nA_{2,n}$, where

$$p_0=-\frac{Bi}{1+Bi} \tag{30}$$

$$p_n=-\frac{Bi+\lambda_n tanh(\lambda_n)}{\lambda_n+Bitanh(\lambda_n)} \tag{31}$$

Using the heat flux conservation interface condition, one may derive

$$A_{2,0}=\frac{\bar{k}_1}{p_0}B_{1,0}=-\frac{\bar{k}_1}{p_0\bar{w}}\int_0^{\bar{w}}\bar{q}(\eta^*)d\eta^* \tag{32}$$

$$A_{2,n}=\bar{k}_1\frac{A_{1,n}sinh(\lambda_n\gamma_1)+B_{1,n}cosh(\lambda_n\gamma_1)}{sinh(\lambda_n\gamma_1)+p_ncosh(\lambda_n\gamma_1)} \tag{33}$$

In eq. (33), $B_{1,n}$ is known already, but $A_{1,n}$ is not known yet. In order to determine $A_{1,n}$ as well as $A_{1,0}$, the interface thermal contact resistance equation is used:

$$A_{1,0}+B_{1,0}\gamma_1+\sum_{n=1}^{N}\left(A_{1,n}cosh(\lambda_n\gamma_1)+B_{1,n}sinh(\lambda_n\gamma_1)\right)cos(\lambda_n\eta)=A_{2,0}+B_{2,0}\gamma_1+\sum_{n=1}^{N}\left(A_{2,n}cosh(\lambda_n\gamma_1)+B_{2,n}sinh(\lambda_n\gamma_1)\right)cos(\lambda_n\eta)-\bar{k}_1\bar{g}_m(\eta)\left[B_{1,0}+\sum_{n=1}^{N}\lambda_n\left(A_{1,n}sinh(\lambda_n\gamma_1)+B_{1,n}cosh(\lambda_n\gamma_1)\right)cos(\lambda_n\eta)\right] \tag{34}$$

Simply integrating eq. (34) results in

$$A_{1,0}\bar{w}+\sum_{n=1}^{N}A_{1,n}\bar{k}_1\lambda_nsinh(\lambda_n\gamma_1)\int_0^{\bar{w}}\bar{g}_1(\eta^*)cos(\lambda_n\eta^*)d\eta^*=\left[\left(\frac{\bar{k}_1}{p_0}+(\bar{k}_1-1)\gamma_1\right)\bar{w}-\int_0^{\bar{w}}\bar{k}_1\bar{g}_1(\eta^*)d\eta^*\right]B_{1,0}-\sum_{n=1}^{N}B_{1,n}\bar{k}_1\lambda_ncosh(\lambda_n\gamma_1)\int_0^{\bar{W}}\bar{g}_1(\eta^*)cos(\lambda_n\eta^*)d\eta^* \tag{35}$$

In eq. (33), $B_{1,0}$ and $B_{1,n}$ are already known from eqs. (18) and (19), respectively, and, therefore, the right-hand side comprises all known quantities, whereas $A_{1,0}$ and $A_{1,n}$ appearing on the left-hand side are unknowns.

Additionally, eq. (34) is multiplied by $\cos(\lambda_{n'}\eta)$ (n' = 1, 2.. N) and then integrated, resulting in

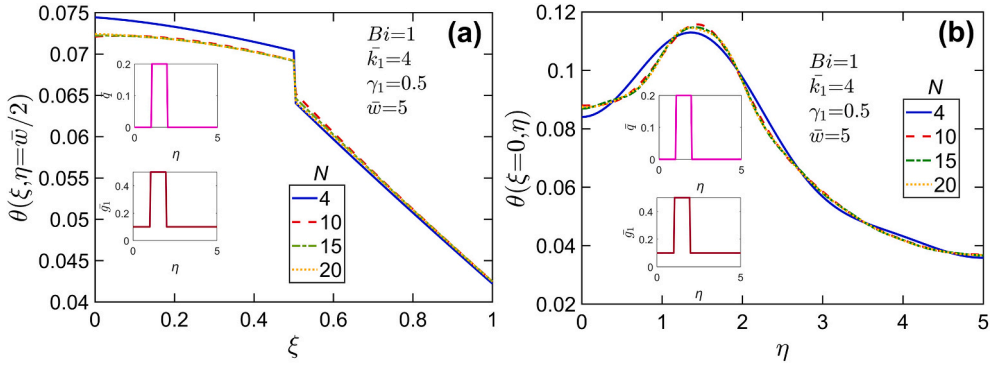

Fig. 2. Effect of number of eigenvalues on temperature distributions: (a) θ as a function of ξ at $\eta = \bar{w}/2$ for multiple number of eigenvalues; (b) θ as a function of η at ξ =0 for multiple number of eigenvalues. Problem parameters are $\bar{w} = 5$, $\bar{k}_1 = 4$, $\gamma_1 = 0.5$, $Bi = 1$. The heat flux $\bar{q}(\eta)$ has a value of 0.2 between η=0.2$\bar{w}$ and η=0.4$\bar{w}$, and zero elsewhere. Thermal contact resistance $\bar{g}_1(\eta)$ has a value of 0.5 between η=0.2$\bar{w}$ and η=0.4$\bar{w}$, and 0.1 elsewhere.

$$A_{1,n'}\left[-\bar{k}_1 sinh(\lambda_{n'}\gamma_1)\frac{cosh(\lambda_{n'}\gamma_1)+p_{n'}sinh(\lambda_{n'}\gamma_1)}{p_{n'}cosh(\lambda_{n'}\gamma_1)+sinh(\lambda_{n'}\gamma_1)}+cosh(\lambda_{n'}\gamma_1)\right]N_{n'}+\sum_{n=1}^{N}A_{1,n}\bar{k}_1\lambda_n sinh(\lambda_n\gamma_1)\int_0^{\bar{w}}\bar{g}_1(\eta^*)cos(\lambda_{n'}\eta^*)cos(\lambda_n\eta^*)d\eta^*$$
$$=-B_{1,0}\bar{k}_1\int_0^{\bar{w}}\bar{g}_1(\eta^*)cos(\lambda_{n'}\eta^*)d\eta^*-\sum_{n=1}^{N}B_{1,n}\bar{k}_1\lambda_n cosh(\lambda_n\gamma_1)\int_0^{\bar{w}}\bar{g}_1(\eta^*)cos(\lambda_{n'}\eta^*)cos(\lambda_n\eta^*)d\eta^*+B_{1,n'}\left[cosh(\lambda_{n'}\gamma_1)\frac{cosh(\lambda_{n'}\gamma_1)+p_{n'}sinh(\lambda_{n'}\gamma_1)}{p_{n'}cosh(\lambda_{n'}\gamma_1)+sinh(\lambda_{n'}\gamma_1)}-sinh(\lambda_{n'}\gamma_1)\right]N_{n'} \quad (36)$$

Eq. (36) may be written for each $n' = 1, 2, .. N$. Therefore, eqs. (35) and (36) constitute $(N + 1)$ equations in $(N + 1)$ unknowns, $A_{1,0}$ and $A_{1,n'}$. These equations are a set of linear, algebraic equations, which can be easily solved using methods such as matrix inversion. In the present work, matrix inversion is carried out using LU decomposition. Once $A_{1,0}$ and $A_{1,n'}$ are determined, the values of these and other coefficients fully determine the temperature distribution, as given by eq. (29).

4. Results and discussion

Given the non-dimensionalization carried out in this work, it is important to first estimate the typical values of key parameters pertaining to this problem. In the context of a multilayer semiconductor chip, the magnitudes of non-dimensional thermal contact resistance $\bar{g}_m(\eta)$ and non-dimensional heat flux $\bar{q}(\eta)$ may be estimated as follows: Firstly, $\bar{g}_m(\eta) = \frac{R_m(y)k_M}{z_M}$. Typical thickness of a multilayer chip stack is around 1–2 mm, and thermal conductivity is of the order of 100 W/mK. Past work has also reported thermal contact resistance in a multilayer chip stack to be of the order of 10^{-5} Km^2/W [10,16]. Based on these numbers, the magnitude of $\bar{g}_m$ is estimated to be 0.5–1, with greater values expected in case of larger thermal contact resistance or a thinner stack. Further, in the context of $\bar{q}(\eta)$, while heat fluxes in a semiconductor chip vary widely, a representative estimate of 10 W/cm^2 may be used. Based on other parameter values described above, and assuming T_{ref} -T_{amb}= 10 K, one may obtain an order of magnitude estimate of $\bar{q}$ to be around 2. Other parameters of this problem, such as $\bar{k}_m$ and γ_m depend on thermal conductivities and thicknesses, respectively, of the layers relative to each other. The aspect ratio $\bar{w}$ depends on the specific chip type, but is usually quite large (a typical semiconductor chip may be only a few mm thick at most several mm wide). Finally, Bi depends on the nature of cooling at the end of the stack, and may vary from a very small value representing poor cooling to a very large value representing excellent cooling, in which case, the boundary approaches isothermal conditions. Parameter values in the typical range based on this discussion are used in all subsequent analysis and plots.

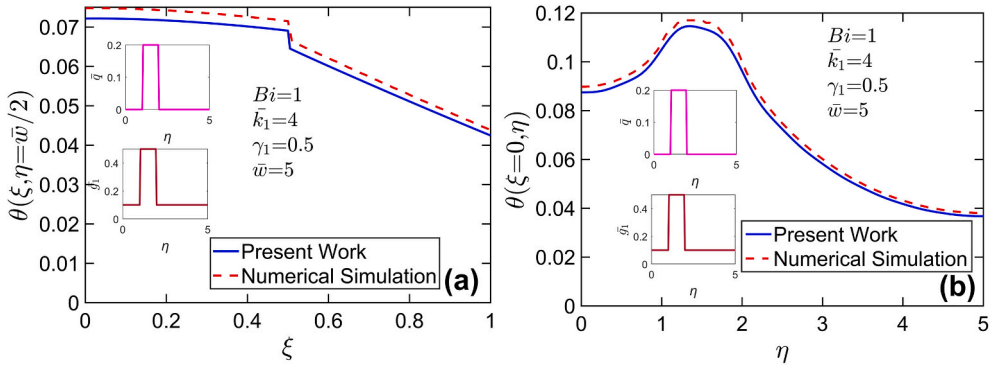

Fig. 3. Comparison of present work with numerical simulations: (a) θ as a function of ξ at $\eta = \bar{w}/2$, (b) θ as a function of η at $\xi = 0$. Curves corresponding to the present analytical model and a finite-element numerical simulation are presented. Problem parameters are identical to Fig. 2.

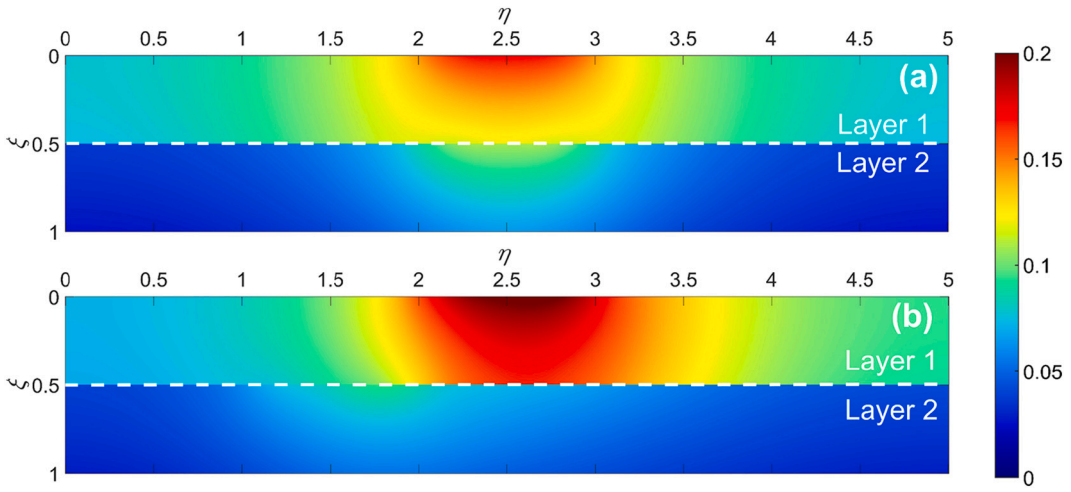

Fig. 4. Illustrative temperature colorplots for two representative cases: (a) $\bar{q}(\eta)$ and $\bar{g}_1(\eta)$ step functions are aligned ($\bar{q}(\eta) = 0.2$ between η=0.4$\bar{w}$ and η=0.6$\bar{w}$, and zero elsewhere, $\bar{g}_1(\eta) = 0.1$ between η=0.4$\bar{w}$ and η=0.6$\bar{w}$, and 2.0 elsewhere); and (b) $\bar{q}(\eta)$ and $\bar{g}_1(\eta)$ step functions are not aligned ($\bar{q}(\eta)$ is the same as Case A, and $\bar{g}_1(\eta) = 0.1$ between η=0.2$\bar{w}$ and η=0.4$\bar{w}$, and 2.0 elsewhere.) Problem parameters are $\bar{w} = 5$, $\bar{k}_1 = 1.5$, $Bi = 1$, $\gamma_1 = 0.5$.

4.1. Effect of number of eigenvalues

A key premise behind the method used in this work is to consider only the first N terms of the infinite series that represents the temperature distribution. This enables calculation of the coefficients appearing in the first N terms of the series by writing sufficient number of linear algebraic equations. It is, therefore, important to examine the impact of the number of terms considered on the accuracy of the solution. In general, the greater the number of terms considered, the more accurate is the solution expected to be, at the cost of increased computational time. Some infinite series converge very slowly [28], and, therefore, it is important to determine the minimum value of N that offers a desirable trade-off between accuracy and computational cost for the present problem.

Towards this goal, Fig. 2 presents the computed temperature distribution as a function of the number of eigenvalues for a representative two-layer problem. Problem parameters used in this plot are $\bar{w} = 5, \bar{k}_1 = 4, \gamma_1 = 0.5$ and $Bi = 1$. In addition, the thermal contact resistance $\bar{g}_1$ and heat flux $\bar{q}$ have values of 0.5 and 0.2, respectively between $\eta = 0.2\bar{w}$ and $\eta = 0.4\bar{w}$, as shown in the insets of Fig. 2. Outside this range, $\bar{g}_1 = 0.1$ and $\bar{q} = 0$. Fig. 2(a) plots the temperature field across both layers at $\eta = \bar{w}/2$, while Fig. 2(b) plots the temperature at the top face ($\xi = 0$) as a function of η. In both cases, temperature curves are plotted for several values of N. Note the discontinuity in the curves shown in Fig. 2(a), which is consistent with the non-zero thermal contact resistance assumed here. These results indicate that for this set of parameter values, the series solution derived in this work converges quite rapidly. There is negligible change in the temperature curve beyond the N=15 case. Even with only four eigenvalues, the temperature distribution incurs only an error of around 4%, which may be acceptable for many engineering problems. Note that there is only minor increase in computational cost in going from 4 to 15 eigenvalues, since solving a set of 15 linear algebraic equations in 15 unknowns is computationally quite straightforward. As a result, all subsequent results presented in this work utilize 15 eigenvalues.

4.2. Model verification using numerical simulation

For increased confidence in the accuracy of the technique used in this work, the analytical model is compared with numerical simulations carried out in a commercial finite-element analysis software. Mesh independence of the numerical simulations is verified in advance. The values of all problem parameters, including heat flux and thermal contact resistance functions are the same as Fig. 2. For this case, Fig. 3(a) and 3(b) plot temperature as a function of ξ at $\eta = \bar{w}/2$, and as a function of η at $\xi = 0$, respectively. In both cases, curves corresponding to the analytical model and the numerical simulation are both plotted. This comparison shows very good agreement between the two, with a worst-case deviation of only 3.5% between the two. Both predict, as expected, a peak in temperature at the center of the heat flux function (Fig. 3(b)), as well as a temperature discontinuity between the two layers due to the thermal contact resistance (Fig. 3(a)).

Note that the analytical technique developed in this work offers several key advantages compared to numerical simulations. Firstly, the analytical solution offers a much better understanding of the fundamental nature of the problem, including identification of key non-

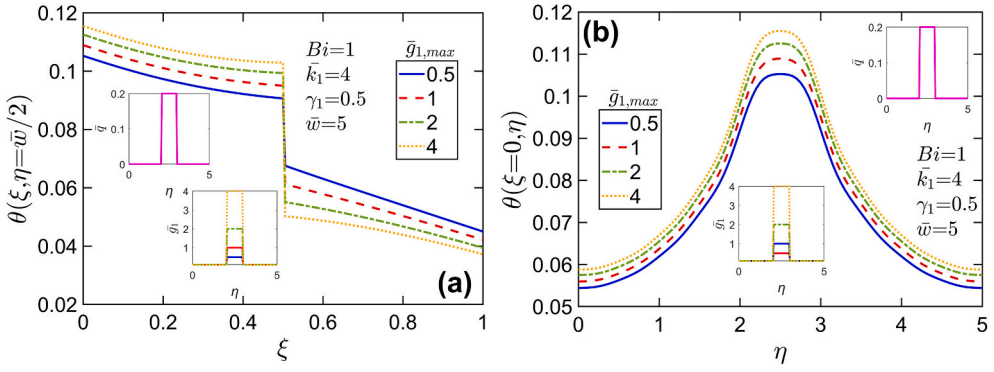

Fig. 5. Effect of contact resistance magnitude when $\bar{q}(\eta)$ and $\bar{g}_1(\eta)$ step functions are aligned ($\bar{g}_1(\eta)$ has a maximum value of $\bar{g}_{1,max}$ between η=0.4$\bar{w}$ and η=0.6$\bar{w}$ and is 0.1 everywhere else. The heat flux, $\bar{q}(\eta)$ has a value of 0.2 between η=0.4$\bar{w}$ and η=0.6$\bar{w}$, and zero everywhere else): (a) θ as a function of ξ at $\eta = \bar{w}/2$ for multiple values of $\bar{g}_{1,max}$ between η=0.4$\bar{w}$ and η=0.6$\bar{w}$, (b) θ as a function of η at ξ =0 for multiple values of $\bar{g}_{1,max}$ between η=0.4$\bar{w}$ and η=0.6$\bar{w}$. Other problem parameters are identical to Fig. 2.

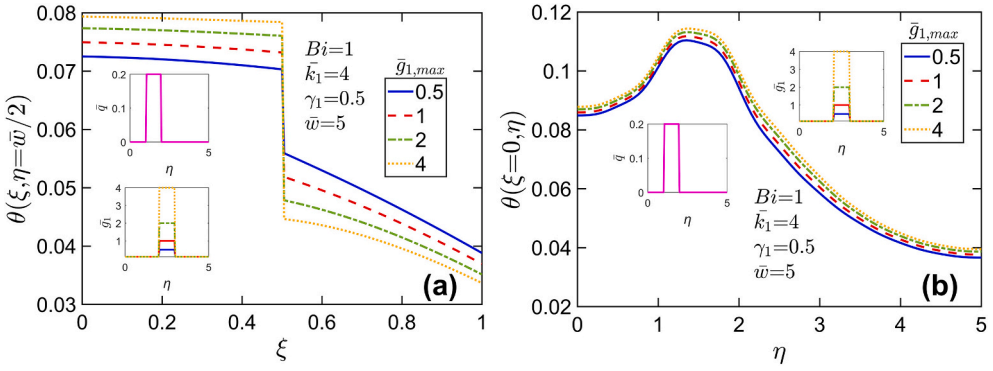

Fig. 6. Effect of contact resistance magnitude when $\bar{q}(\eta)$ and $\bar{g}_1(\eta)$ step functions are not aligned ($\bar{g}_1(\eta)$ has a value of $\bar{g}_{1,max}$ between η=0.4$\bar{w}$ and η=0.6$\bar{w}$ and is 0.1 everywhere else. $\bar{q}(\eta)$ has a value of 0.2 between η=0.2$\bar{w}$ and η=0.4$\bar{w}$, and zero everywhere else): (a) θ as a function of ξ at $\eta = \bar{w}/2$ for multiple values of $\bar{g}_{1,max}$ between η=0.4$\bar{w}$ and η=0.6$\bar{w}$, (b) θ as a function of η at $\xi = 0$ for multiple values of $\bar{g}_{1,max}$ between η=0.4$\bar{w}$ and η=0.6$\bar{w}$. Other problem parameters are identical to Fig. 2.

dimensional parameters and their dependence on each other. From a practical perspective, computation of the analytical solution is much simpler than numerical simulations, since only a few terms in the series have been shown in the previous sub-section to result in good accuracy. Using the analytical solution, temperature can be computed only at desired locations instead of having to solve the entire temperature field in a numerical simulation. Further, numerical simulations often require proprietary software, and mesh generation can be time consuming. As a comparison, the typical time taken for temperature computation using the analytical method is found to be less than 2.6 s, compared to over a minute for the numerical simulation to converge, without even accounting for the time taken for setting up the geometry and mesh generation.

4.3. Illustrative temperature maps

Fig. 4 presents temperature maps computed using the analytical model for a typical two-layer geometry. Two cases of practical importance are considered. In both cases, $\bar{g}_1$ and $\bar{q}$ are considered to be step functions, as is likely to be the case in practical devices. However, (a) and (b) consider cases in which the two step functions are either aligned with each other or not. In case (a), the $\bar{q}$ step function is 0.2 between $\eta = 0.4\bar{w}$ and $\eta = 0.6\bar{w}$, and zero elsewhere, whereas $\bar{g}_1$ has a low value of 0.1 between $\eta = 0.4\bar{w}$ and $\eta = 0.6\bar{w}$ and a high value of 2.0 outside this range. In case (b), the low region for $\bar{g}_1$ lies between $\eta = 0.2\bar{w}$ and $\eta = 0.4\bar{w}$, resulting in misalignment between $\bar{g}_1$ and $\bar{q}$. Such scenarios may occur in practical semiconductor devices where the heat-generating circuit block is misaligned or aligned with the low thermal resistance region at the interface (which could be due to a large number of through-silicon vias in that region). Except $\bar{k}_1 = 1.5$, all other problem parameter values considered here are the same as Fig. 2. The temperature colormap for case (a) presented in Fig. 4(a) clearly shows, as anticipated, greater penetration into layer 2 due to alignment of the imposed heat flux region with the lower thermal contact resistance region. In Fig. 4(b), on the other hand, the penetration is less significant and shifts to the new position of lower thermal resistance region. In other words, the alignment in Fig. 4(a) increases the maximum temperature of layer 2, and reduces the maximum temperature observed in layer 1. On the other hand, misalignment of $\bar{g}_1$ and $\bar{q}$ increases the maximum temperature of layer 1. In practical semiconductor chips, the peak temperature is of most interest, as it determines device reliability. Therefore, it is desirable to align the high heat-generating regions with low thermal contact resistance regions at the interface.

Note that the temperature colormap for case (a) presented in Fig. 4 (a) clearly shows a symmetric temperature distribution about $\eta = 0.5\bar{w}$, which is expected due to symmetry in the problem. On the other hand, the temperature distribution in case (b) is no longer symmetric, as expected.

4.4. Effect of contact resistance magnitude

The impact of magnitude of the thermal contact resistance on temperature distribution is investigated next. With the problem parameters as Fig. 2, temperature distribution is plotted for a number of cases with different magnitudes of $\bar{g}_1$, modeled to be a top hat function that is aligned to the peak heat flux region. Resulting temperature curves are shown in Fig. 5, in which, $\bar{g}_1$ and $\bar{q}$ functions are shown as insets. While temperature distribution across both layers at the center of the geometry ($\eta = 0.5\bar{w}$) is presented in Fig. 5(a), temperature distribution on the heat flux face ($\xi = 0$) is shown in Fig. 5(b). Cases corresponding to $\bar{g}_{1,max} = 0.5, 1.0, 2.0, 4.0$ are presented. Fig. 5(a) shows, as expected, that the temperature jump at the interface grows as the value of $\bar{g}_{1,max}$ increases, along with an increase in temperature distribution in the first layer. The temperature distribution on the heat flux face, presented in Fig. 5(b),

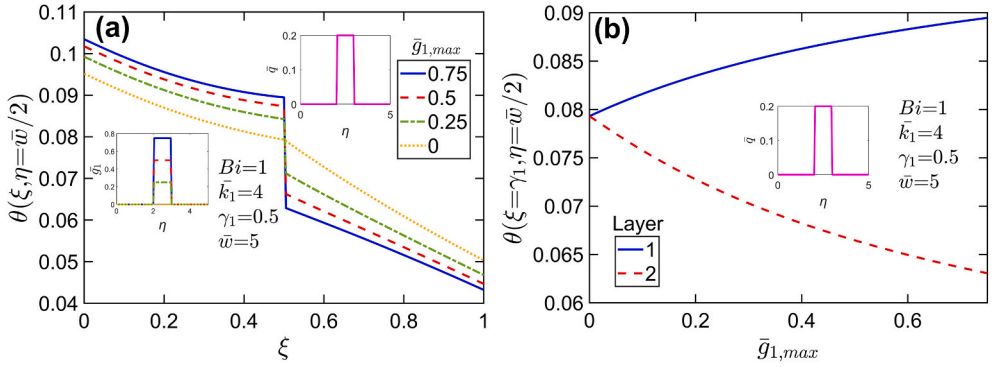

Fig. 7. Effect of gradually reducing $\bar{g}_{1,max}$ to zero: (a) θ as a function of ξ at $\eta = \bar{w}/2$, (b) θ as a function of $\bar{g}_{1,max}$ at ξ=$\gamma_1$and $\eta = \bar{w}/2$ for layers 1 and 2. The heat flux, $\bar{q}(\eta)$ has a value of 0.2 between η=0.4$\bar{w}$ and η=0.6$\bar{w}$, and zero everywhere else. $\bar{q}(\eta)$ and $\bar{g}_1(\eta)$ step functions are aligned. Other problem parameters are identical to Fig. 2.

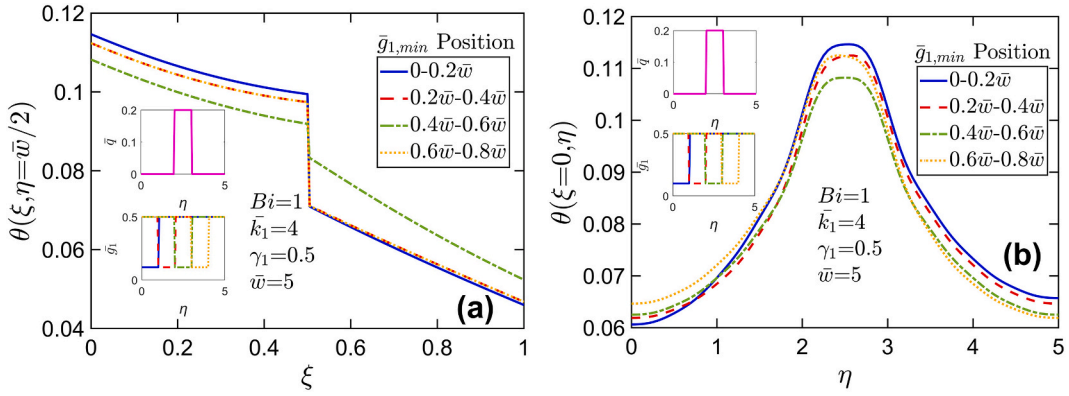

Fig. 8. Effect of alignment between $\bar{q}(\eta)$ and $\bar{g}_1(\eta)$ step functions: (a) θ as a function of ξ at $\eta = \bar{w}/2$ for multiple positions of $\bar{g}_{1,min}$, (b) θ as a function of η at $\xi = 0$ for multiple positions of $\bar{g}_{1,min}$. Contact resistance has a value of 0.5 everywhere else. $\bar{q}(\eta) = 0.2$ between η=0.4$\bar{w}$ and η=0.6$\bar{w}$, and zero elsewhere. Other problem parameters are identical to Fig. 2.

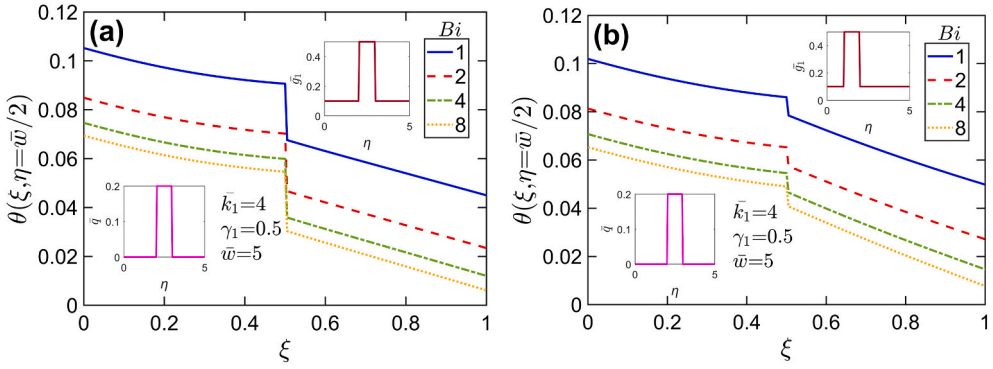

Fig. 9. Effect of Bi for two distinct cases: θ as a function of ξ at $\eta = \bar{w}/2$ for multiple values of Bi when $\bar{q}(\eta)$ and $\bar{g}_1(\eta)$ step functions are (a) aligned; (b) not aligned. In case (a), $\bar{g}_1(\eta) = 0.5$ between η=0.4$\bar{w}$ and η=0.6$\bar{w}$, and 0.1 elsewhere, and in case (b), $\bar{g}_1(\eta) = 0.5$ between η=0.2$\bar{w}$ and η=0.4$\bar{w}$, and 0.1 elsewhere. In both cases, $\bar{q}(\eta) = 0.2$ between η=0.4$\bar{w}$ and η=0.6$\bar{w}$, and zero elsewhere. Other problem parameters are identical to Fig. 2.

shows in each case, as expected, that the highest temperature occurs at the center of the region of the applied heat flux. Further, the shapes of the temperature curves for each case are similar, and there is an increase in the peak temperature rise. This is along expected lines, because the greater the thermal contact resistance, the large would the temperature rise be due to increase in total thermal resistance.

Fig. 6 presents similar plots, with the key difference that, in this case, the heat flux and thermal interface resistance distributions are not aligned with each other, similar to Fig. 4(b). Fig. 6(a) shows similar increase in temperature discontinuity with increasing $\bar{g}_{1,max}$ as Fig. 5(a). Temperature drop at the interface is lower for Fig. 6(a) compared to Fig. 5(a), which is because in Fig. 5(a), the positions of the heat flux and maximum thermal contact resistance are aligned with each other, resulting in symmetric flow of heat through regions containing lower thermal contact resistance, and thereby causing higher temperature drop. However, Fig. 6(b) shows that the peak temperature rise in this case is no longer much sensitive to $\bar{g}_{1,max}$. This demonstrates that alignment or misalignment of heat flux distribution and the distribution of thermal contact resistance may play a key role in determining the peak temperature distribution in the semiconductor chip. A shift in the location of the peak temperature rise in Fig. 6(b) compared to Fig. 5(b) may also be noted, which is because of the shift in the $\bar{q}$ distribution. In both Figs. 5(b) and 6(b), it can be noticed that the slope of the temperature distribution is zero at η=0 and η=$\bar{w}$, which is in line with the corresponding boundary conditions at those boundaries.

The impact of $\bar{g}_{1,max}$ on the resulting temperature distribution is further investigated in Fig. 7. Temperature curves are plotted for four cases of gradually decreasing $\bar{g}_{1,max}$, including the limiting case of $\bar{g}_{1,max} = 0$, corresponding to zero thermal contact resistance. Fig. 7(a) plots temperature as a function of ξ at η=$\bar{w}/2$, whereas Fig. 7(b) plots the temperatures of layers 1 and 2 at the middle of the interface ($\xi = \gamma_1, \eta = \bar{w}/2$) as a function of $\bar{g}_{1,max}$. $\bar{g}_1$ and $\bar{q}$ functions are indicated

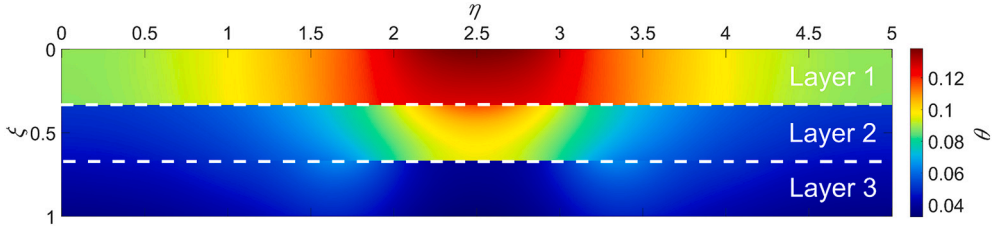

Fig. 10. Illustrative 2D colorplot of temperature distribution for a three-layer case. $\bar{q}(\eta), \bar{g}_1(\eta)$ and $\bar{g}_2(\eta)$ are step functions as described in the text. Other problem parameters are $\bar{w}$=5, $\bar{k}_1$=4, $\bar{k}_2$=2, γ_1=0.25, γ_2=0.75, Bi=1.

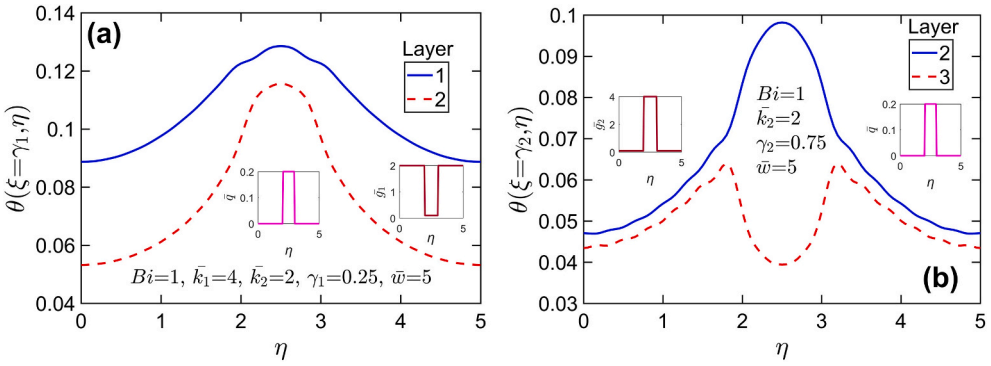

Fig. 11. θ vs η for a three-layer case: (a) at $\xi = \gamma_1$, (b) at $\xi = \gamma_2$. $\bar{q}(\eta), \bar{g}_1(\eta)$ and $\bar{g}_2(\eta)$ are step functions as described in the text. Other problem parameters are $\bar{w}$=5, $\bar{k}_1$=4, $\bar{k}_2$=2, γ_1=0.25, γ_2=0.75, Bi=1.

in inset of Fig. 7(a). Fig. 7(a) shows that as $\bar{g}_{1,max}$ reduces, both temperature magnitudes as well as the temperature discontinuity at the interface reduce. This is expected, because the lower the value of $\bar{g}_{1,max}$, the lower is the interface resistance (responsible for the magnitude of interfacial temperature discontinuity) as well as the total thermal resistance (responsible to total temperature rise). The limiting case of $\bar{g}_{1,max} = 0$ corresponds to zero interface resistance, leading to a continuous temperature curve across the interface, as shown in Fig. 7(a). Temperatures in the two layers at the middle of the interface, plotted in Fig. 7(b) as functions of $\bar{g}_{1,max}$ show that as the maximum contact resistance increases, the temperatures diverge away from each other. For the limiting case of $\bar{g}_{1,max} = 0$, the two are equal to each other, as expected.

4.5. Effect of location of thermal resistance

The effect of alignment between step functions of $\bar{g}_1$ and $\bar{q}$ is specifically analyzed through Fig. 8 with all the other problem parameters remaining unchanged. To present this Figure in terms of temperature distribution along the layered direction at η=$\bar{w}/2$ and along the η-direction at ξ=0, the imposed heat flux is fixed between 0.4$\bar{w}$ and 0.6$\bar{w}$ and the position of $\bar{g}_{1,min}$ is varied. The different positions considered for this analysis are 0–0.2$\bar{w}$, 0.2$\bar{w}$-0.4$\bar{w}$, 0.4$\bar{w}$-0.6$\bar{w}$ and 0.6$\bar{w}$-0.8$\bar{w}$. In Fig. 8(a), temperature drop at the interface is the highest for $\bar{g}_{1,min}$ between 0 and 0.2$\bar{w}$, which is along expected lines since the path of least resistance is located far away from the imposed heat flux region. As the position of $\bar{g}_{1,min}$ is brought closer to the imposed heat flux region, the temperature distribution in layer 1 drops, whereas the temperature distribution in layer 2 rises. Evidently, the temperature drop at the interface is the lowest when $\bar{g}_{1,min}$ and the imposed heat flux region are aligned, as expected. Finally, symmetry can be observed for the cases of 0.2$\bar{w}$-0.4$\bar{w}$ and 0.6$\bar{w}$-0.8$\bar{w}$ $\bar{g}_{1,min}$ positions. In Fig. 8(b), it can be observed that maximum temperature is encountered when $\bar{g}_{1,min}$ is located far away from the imposed heat flux region, as expected. As the position of $\bar{g}_{1,min}$ is moved closer to the imposed heat flux region, the magnitude of maximum temperature drops which is a consequence of aligning the lower thermal resistance region with the imposed heat flux region. The curve corresponding to 0.6$\bar{w}$-0.8$\bar{w}$ $\bar{g}_{1,min}$ position is a mirror image of the 0.2$\bar{w}$-0.4$\bar{w}$ $\bar{g}_{1,min}$ position curve, as expected from symmetry arguments.

4.6. Impact of biot number

The Biot number is another important non-dimensional parameter in this problem. The magnitude of Bi governs the extent of cooling at the ξ = 1 face. Fig. 9 plots temperature curves along the layered direction at $\eta = \bar{w}/2$ for two cases – in the first case, plotted in Fig. 9(a), the step functions associated with the heat flux and thermal contact resistance are centrally aligned (between $\eta = 0.4\bar{w}$ and $\eta = 0.6\bar{w}$), and in the second case (Fig. 9(b)), there is an offset, such that $\bar{g}_{1,max}$ exists between $\eta = 0.2\bar{w}$ and $\eta = 0.4\bar{w}$. Other problem parameters are the same as previous problems. In both cases, temperature curves are plotted for different values of Bi. As expected, both Figures show that an increase in Bi results in a reduction in temperature rise, due to more effective convective cooling. In both cases, a saturation effect is also seen, wherein, there is significant reduction in temperature when Bi increases from a value of 1 to 2, but the impact is relatively smaller at greater values of Bi, for example, between the $Bi = 4$ and $Bi = 8$ curves. As expected, the magnitude of temperature discontinuity does not change with Bi, which is because of its dependence on the nature of the thermal contact resistance rather than Bi. Temperature drop at the interface for each case in Fig. 9(a) is higher as a result of alignment between the imposed heat flux and thermal contact resistance step functions. Movement of $\bar{g}_{1,max}$ away from the imposed heat flux region results in a lower resistance path, causing the temperature drop to be lower at the interface in Fig. 9 (b), similar to the observation made in the previous Figure.

4.7. Results for three-layer case

Finally, results for a more complicated, three-layer case are presented. This case comprises two distinct thermal contact resistance functions – $\bar{g}_1(\eta)$ between layers 1 and 2, and $\bar{g}_2(\eta)$ between layers 2 and 3. For $\bar{w}$=5, $\bar{k}_1$=4, $\bar{k}_2$=2, γ_1=0.25, γ_2=0.75 and $Bi = 1$, Fig. 10 presents a colorplot of the computed temperature distribution, whereas Figs. 11(a) and 11(b) plot temperature as a function of η along the two interfaces. $\bar{g}_1, \bar{g}_2$ and $\bar{q}$ are step functions that are aligned with each other. Similar to preceding Figures, $\bar{q} = 0.2$ between $\eta = 0.4\bar{w}$ and $\eta = 0.6\bar{w}$, and zero elsewhere. The first thermal interface resistance $\bar{g}_1$ has a low value of 0.1 between $\eta = 0.4\bar{w}$ and $\eta = 0.6\bar{w}$ and a high value of 2.0 elsewhere. $\bar{g}_2$ has a high value of 4.0 between $\eta = 0.4\bar{w}$ and $\eta = 0.6\bar{w}$. Elsewhere, $\bar{g}_2$ has a value of 0.01 and 0.1 for Figs. 10 and 11, respectively. Fig. 10 clearly shows thermal penetration into layer 2 from layer 1 in the region between $\eta = 0.4\bar{w}$ and $\eta = 0.6\bar{w}$, which is the region corresponding to lower thermal resistance. On the other hand, at the second interface, the penetration shifts to other regions of the body. This is attributed to the presence of a very high thermal resistance in the same region. Fig. 11(a) shows the interfacial temperature distributions for layers 1 and 2 approach each other between $\eta = 0.4\bar{w}$ and $\eta = 0.6\bar{w}$, and deviate from each other elsewhere, which is consistent with the nature of $\bar{g}_1(\eta)$. The opposite effect can be noticed in Fig. 11(b), in which, there is a relatively large interfacial temperature drop between $\eta = 0.4\bar{w}$ and $\eta = 0.6\bar{w}$ due to higher thermal resistance in that region. Elsewhere, the temperature curves are quite close to each other, due to lower interface resistance in those regions. Curves such as those presented in Figs. 11(a) and 11(b) may be useful for understanding the connection between interfacial thermal contact resistance distribution due to the design of chip features

such as TSVs and bond pads with the resulting temperature distribution.

5. Conclusions

The key contribution of the analytical model presented in this work is the capability to account for spatially-varying thermal contact resistance distributions at multiple interfaces in a multi-layer semiconductor chip. This problem can not be solved with standard analytical tools, and the technique utilized here generalizes much of past work, which only modeled a constant thermal contact resistance. The analytical model can be computed much faster than numerical simulations, and also offers a better fundamental understanding of the heat transfer problem. Spatial variation in thermal contact resistance may arise due to practical features in the chip architecture, as discussed in prior sections, and, therefore, the present work may be of much practical relevance.

While presented as a two-dimensional problem, extension to a three-dimensional problem is quite straightforward. In such a case, both directions normal to the thickness direction will contribute one set of eigenvalues each, and the temperature distribution will be given by a double summation. The problem will involve a greater number of unknown coefficients, but these can continue to be determined using the technique described here.

This work derives an analytical solution for the steady state problem, which can not be directly used for analyzing transient problems. Specifically, transient thermal response to changes in the heat load can not be modeled using this technique. While steady state analysis is often sufficient for thermal design of semiconductor chips, this is identified as a key limitation of the present work. Note that transient problems can be solved by Laplace transformation followed by solution of the problem in Laplace domain similar to the technique described here. Further, the solution derived here may incur error when considering problems with very large temperature rise due to assumption of constant thermal properties. This is usually not the case for semiconductor thermal management.

While discussed in the context of semiconductor thermal management, multilayer heat transfer is relevant to several other engineering applications as well. It is expected that the theoretical technique presented here may be of relevance in such applications involving spatially varying thermal contact resistances.

CRediT authorship contribution statement

Girish Krishnan – Conceptualization, Formal Analysis, Investigation, Data Curation, Visualization; Ankur Jain – Conceptualization, Methodology, Supervision, Project Administration. All authors contributed towards writing original draft and review/editing.

Declaration of Competing Interest

None.

Data availability

Data will be made available on request.

References

[1] S.V. Garimella, et al., Thermal challenges in next generation electronic systems - summary of panel presentations and discussions, IEEE Trans. Components Packag. Technol. 25 (4) (2002) 569–575, https://doi.org/10.1109/TCAPT.2003.809113.
[2] S.S. Salvi, A. Jain, A review of recent research on heat transfer in three-dimensional integrated circuits (3-D ICs), IEEE Trans. Compon. Packag. Manuf. Technol. 11 (5) (2021) 802–821, https://doi.org/10.1109/TCPMT.2021.3064030.
[3] R.C. Chu, R.E. Simons, M.J. Ellsworth, R.R. Schmidt, V. Cozzolino, Review of cooling technologies for computer products, IEEE Trans. Device Mater. Reliab. 4 (4) (2004) 568–585, https://doi.org/10.1109/TDMR.2004.840855.
[4] R. Mahajan, C.P. Chiu, G. Chrysler, Cooling a microprocessor chip, Proc. IEEE 94 (8) (2006) 1476–1485, https://doi.org/10.1109/JPROC.2006.879800.
[5] D.B. Tuckerman, R.F.W. Pease, High-performance heat sinking for VLSI, IEEE Electron Dev. Lett. 2 (5) (1981) 126–129, https://doi.org/10.1109/EDL.1981.25367.
[6] S.G. Kandlikar, Review and projections of integrated cooling systems for three-dimensional integrated circuits, J. Electron. Packag. Trans. ASME 136 (2) (2014), https://doi.org/10.1115/1.4027175.
[7] V. Venkatadri, B. Sammakia, K. Srihari, D. Santos, A review of recent advances in thermal management in three dimensional chip stacks in electronic systems, J. Electron. Packag. 133 (2011), 041011, https://doi.org/10.1115/1.4005298.
[8] R. Schaller, Moore's law: past, present and future, IEEE Spectr. 34 (1997) 52–59, https://doi.org/10.1109/6.591665.
[9] K. Banerjee, S.J. Souri, P. Kapur, K.C. Saraswat, 3-D ICs: a novel chip design for improving deep-submicrometer interconnect performance and systems-on-chip integration, Proc. IEEE 89 (5) (2001) 602–633, https://doi.org/10.1109/5.929647.
[10] E.G. Colgan, et al., Measurement of microbump thermal resistance in 3D chip stacks, in: 2012 28th Annual IEEE Semiconductor Thermal Measurement and Management Symposium (SEMI-THERM), 2012, pp. 1–7, https://doi.org/10.1109/STHERM.2012.6188818.
[11] H. Oprins, V. Cherman, B. Vandevelde, C. Torregiani, M. Stucchi, G. der Plas, P. Marchal, E. Beyne, Characterization of the thermal impact of Cu-Cu bonds achieved using TSVs on hot spot dissipation in 3D stacked ICs, in: 2011 IEEE 61st Electronic Components and Technology Conference (ECTC), 2011, pp. 861–868, https://doi.org/10.1109/ECTC.2011.5898612.
[12] L. Choobineh, A. Jain, Analytical solution for steady-state and transient temperature fields in vertically stacked 3-D integrated circuits, IEEE Trans. Compon. Packag. Manuf. Technol. 2 (12) (2012) 2031–2039, https://doi.org/10.1109/TCPMT.2012.2213820.
[13] S. Pozder, R. Chatterjee, A. Jain, Z. Huang, R.E. Jones, E. Acosta, Progress of 3D integration technologies and 3D interconnects, IEEE Int. Interconnect Technol. Conf. (2007) 213–215, https://doi.org/10.1109/IITC.2007.382393.
[14] Z. Huang, R. Chatterjee, P. Justison, et al., Electromigration of Cu-Sn-Cu micropads in 3D interconnect, in: 2008 IEEE Electronic Components and Technology Conference, 2008, pp. 12–17, https://doi.org/10.1109/ECTC.2008.4549943.
[15] S. Pozder, A. Jain, R. Chatterjee, et al., 3D die-to-wafer Cu/Sn microconnects formed simultaneously with an adhesive dielectric bond using thermal compression bonding, IEEE Int. Interconnect Technol. Conf. (2008) 46–48, https://doi.org/10.1109/IITC.2008.4546921.
[16] L. Choobineh, J. Jones, A. Jain, Experimental and numerical investigation of interdie thermal resistance in three-dimensional integrated circuits, J. Electron. Packag. 139 (2) (2017), https://doi.org/10.1115/1.4036404.
[17] J. Geer, A. Desai, B. Sammakia, Heat conduction in multilayered rectangular domains, J. Electron. Packag. 129 (4) (2007) 440–451, https://doi.org/10.1115/1.2804094.
[18] L. Choobineh, A. Jain, An explicit analytical model for rapid computation of temperature field in a three-dimensional integrated circuit (3D IC), Int. J. Therm. Sci. 87 (2015) 103–109, https://doi.org/10.1016/j.ijthermalsci.2014.08.012.
[19] B. Goplen, S.S. Sapatnekar, Placement of thermal vias in 3-D ICs using various thermal objectives, IEEE Trans. Comput. Aid. Des. Integrat. Circuits Syst. 25 (4) (2006) 692–709, https://doi.org/10.1109/TCAD.2006.870069.
[20] J. Cong, G. Luo, J. Wei, Y. Zhang, Thermal-aware 3D IC placement via transformation, in: 2007 Asia and South Pacific Design Automation Conference, 2007, pp. 780–785, https://doi.org/10.1109/ASPDAC.2007.358084.
[21] L. Zhou, M. Parhizi, A. Jain, Theoretical modeling of heat transfer in a multilayer rectangular body with spatially-varying convective heat transfer boundary condition, Int. J. Therm. Sci. 170 (2021), 107156, https://doi.org/10.1016/j.ijthermalsci.2021.107156.
[22] L. Choobineh, A. Jain, Determination of temperature distribution in three-dimensional integrated circuits (3D ICs) with unequally-sized die, Appl. Therm. Eng. 56 (1–2) (2013) 176–184, https://doi.org/10.1016/j.applthermaleng.2013.03.006.
[23] S.W. Ma, A.I. Behbahani, Y.G. Tsuei, Two-dimensional rectangular fin with variable heat transfer coefficient, Int. J. Heat Mass Transf. 34 (1) (1991) 79–85, https://doi.org/10.1016/0017-9310(91)90175-E.
[24] D. Sarkar, K. Shah, A. Haji-Sheikh, A. Jain, Analytical modeling of temperature distribution in an anisotropic cylinder with circumferentially-varying convective heat transfer, Int. J. Heat Mass Transf. 79 (2014) 1027–1033, https://doi.org/10.1016/j.ijheatmasstransfer.2014.08.060.
[25] F.P. Incropera, D. DeWitt, T. Bergman, A.S. Levine, Fundamentals of Heat and Mass Transfer, 6th ed., John Wiley & Sons, 2006. ISBN: 978–0471457282.
[26] M.G. Cooper, B. Mikic, M.M. Yovanovich, Thermal contact conductance, Int. J. Heat Mass Transf. 12 (1969) 279–300, https://doi.org/10.1016/0017-9310(69)90011-8.
[27] D.W. Hahn, M.N. Özışık, Heat Conduction, 3rd ed., Wiley, Hoboken, N.J, 2012.
[28] D. Anthony, D. Sarkar, A. Jain, Non-invasive, transient determination of the core temperature of a heat-generating solid body, Sci. Rep. 6 (2016) 1–10, https://doi.org/10.1038/srep35886, pp. 35886.